ICAS-88-3.11.R1

# INVESTIGATIONS ON THE VORTICITY SHEETS OF A CLOSE-COUPLED DELTA-CANARD CONFIGURATION[+)]

Hans-Christoph Oelker, Dietrich Hummel
Institut für Strömungsmechanik, Technische Universität Braunschweig
Bienroder Weg 3, D-3300 Braunschweig

## Abstract

Comprehensive aerodynamic investigations have been carried out on a close-coupled A = 2.31 delta-canard configuration at low speed. Results of three-component, surface-pressure and flow-field measurements as well as oilflow patterns are presented for the canard-off and for the canard-on configuration. The main interference effects take place above the wing: The formation of the wing vortices is delayed considerably to positions downstream of the apex. The canard vortices pass the wing leading-edge relatively high and they are moved downwards and inwards above the wing. During this process a fusion between the canard's vorticity sheet and the suction side boundary layer of the wing takes place in the inner portion of the wing. The canard vortex system is maintained up to stations downstream of the wing trailing-edge.

## 1. Introduction

A close-coupled canard configuration is a characteristic feature of modern fighter aircraft (e.g.: IAI-Lavi, SAAB-Gripen or EFA). The physics of the corresponding three-dimensional and separated flow is therefore of high interest for aeronautical research work. Canard configurations have been investigated for a long time and there exists a large number of publications of experimental work on this topic; however these papers are mainly aimed to find practicable configurations of aircraft design. Publications dealing with the physics of the flow field and the interfering vortex systems from canard and wing are rare. Systematic investigations as well as detailed flow-field measurements are missing until now. In order to fill this gap an extensive research program on close-coupled canard configurations was initiated at Institut für Strömungsmechanik of Technische Universität Braunschweig. The aim is to get detailed insight into the interference between the vortex systems of canard and wing and to provide experimental data for a comparison with theoretical results. In particular it is intended to give a detailed quantitative documentation of the three-dimensional flow field as it was done earlier already for the delta wing and double-delta wings.

It is known since H. Behrbohm[1] in 1965, that close-coupled canard configurations with canard and wing of small aspect ratios in the range of $1 \leq A \leq 3$ have substantial advantages. The value of maximum lift coefficient $c_{L_{max}}$ and the corresponding angle of attack $\alpha(c_{L_{max}})$ can be considerably increased by adding a delta canard to a delta wing. This advantage is due to favourable interference between the vortex systems of canard and wing[1].

In addition to the contribution of H. Behrbohm[1] one can find a lot of papers on canard configurations. An early series of experiments has been carried out at NASA in the 1950's, Refs. 2 to 8, in which long-coupled canard configurations were tested. Later a second series of measurements has been performed at Naval Ship Research and Development Center (NSRDC), Refs. 9 to 12, and a third series at NASA, Refs. 13 to 20. These two last series were concerned with close-coupled canard configurations and were aimed at finding practicable configurations. Other single publications by R.B. Eberle et al.[21] and S.E. Goldstein, C.P. Combs[22] deal with trimming capabilities of close-coupled canard configurations in comparison with conventional configurations. H. John, W. Kraus[23] and W. Kraus[24] investigated the aerodynamics of close-coupled canard configurations also beyond stall. Investigations on the physics of the interfering vortex systems of canard and wing were performed by B.B. Gloss and D.D. Miner[25], D.J. Lorincz[26] as well as by J. Er-El and A. Seginer[27], but these papers mainly give qualitative insight into the flow structure by flow visualization. Quantitative work was done by R. Gallington and G. Sisson[28], K.E. Griffin[29], K.E. Griffin, E.C. Haerter and B.R. Smith[30], K.E. Griffin and F.M. Jonas[31] as well as by L. Hjelmberg[32]. Refs. 26 and 29 to 31 deal with canard configurations which have a forward swept wing. The results of Refs. 28 to 31 are flow-field measurements in symmetrical and incompressible flow. The development of vorticity sheets is not presented. Ref. 32 contains results, which were obtained with the two European models of the "International Vortex Flow Experiment on Euler Code Validation" in symmetrical and compressible flow. L. Hjelmberg's[32] results also do not show the development of vorticity sheets.

The investigations performed at the Institut für Strömungsmechanik of Technische Universität Braunschweig are concerned in two different configurations. Fig.1 shows the sharp-edged delta wing configuration with $A_C = A_W = 2.31$ and $(b_C/b_W)=0.4$. The flat fuselage provides the possibility of varying canard position and attitude relative to the wing systematically. Three-component, surface-pressure and flow-field measurements using a conventional five-hole probe as well as flow visualizations by means of oilflow patterns have been performed in the institute's 1.3-m low speed wind-tunnel. Additional flow visualizations in a small water-tunnel have also been carried out. The investigations were concerned in the wing alone as well as in the canard-wing combination in order to detect interference effects. The achieved results of this survey have already been partly published in Refs. 33, 34

+) These investigations have been supported by DEUTSCHE FORSCHUNGSGEMEINSCHAFT under contract number DFG Hu 254/8

and 35. Further results of flow-field measurements, which show the development of the canard wake over the wing in detail, are being presented here. The second canard configuration under consideration is the configuration of the "International Vortex Flow Experiment on Euler-Code Validation". The investigations on this configuration are under way right now and will be documented in Ref. 36 in the same manner as given in Refs. 33, 34 and here.

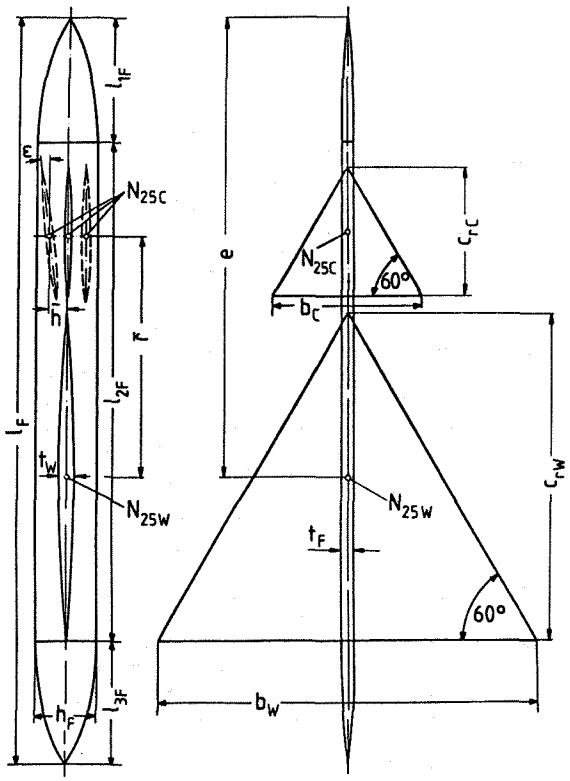


Fig. 1: Wing-fuselage-canard configuration

## 2. Notations (see Fig. 1)

### 2.1 Geometric quantities

| | |
|---|---|
| $A = b^2/S$ | Aspect ratio of canard or wing |
| $H = \bar{h}/c_{rW}$ | Dimensionless vertical position of the canard |
| $N_{25}$ | Geometric neutral point of canard or wing |
| $R = (\bar{r}-\bar{r}_0)/c_{rW}$ | Dimensionless relative forward position of the canard |
| S | Area of canard or wing (extended to $y_C = y_W = 0$ according to Fig. 1) |
| $b = 2s$ | Span of canard or wing |
| $c(y)$ | Local chord of canard or wing |
| $c_r = c(y = 0)$ | Root chord of canard or wing |
| $\bar{c} = \frac{1}{S_W}\int_{-s_W}^{+s_W} c_W^2\, dy_W$ | Mean aerodynamic chord of the wing |
| e | Distance between fuselage apex and wing geometric neutral point |
| $h_F$ | Height of the fuselage |
| $\bar{h}$ | Distance of the canard geometric neutral point $N_{25C}$ from the fuselage axis |
| $l_F$ | Length of the fuselage |
| $l_{1F}, l_{2F}, l_{3F}$ | Length of front, cylindrical and rear part of the fuselage |
| $\bar{r}$ | Horizontal distance between the geometric neutral points of canard and wing |
| $\bar{r}_0 = (c_{rW}+c_{rC})/2$ | Horizontal distance between the geometric neutral points of canard and wing for canard trailing-edge located at wing apex |
| s | Half span of canard or wing |
| $s_1(x)$ | Local half span of canard or wing |
| t | Maximum thickness of canard or wing or fuselage |
| x,y,z | Body-fixed coordinates, origin at canard or wing apex |
| $x_{N25} = c_r/2$ | Distance of geometric neutral point from origin of coordinate system for wing or canard |
| $\varepsilon$ | Setting angle of the canard; angle between the planes of canard and wing |
| $\xi = x/c_r$ | Dimensionless body-fixed coordinate for canard or wing |
| $\eta = y/s_1$ | Dimensionless local spanwise coordinate for canard or wing |
| $\tilde{\eta}_W = y_W/s_{1W}$<br>$\tilde{\zeta}_W = z_W \cdot \cos\alpha/s_{1W}$ | Dimensionless aerodynamic coordinates with the origin at the intersection of the measuring plane and the $x_W$-axis |
| $\bar{\eta}_W = y_W/s_W$<br>$\bar{\zeta}_W = z_W \cdot \cos\alpha/s_W$ | Dimensionless aerodynamic coordinates with the origin at the intersection of the measuring plane with an axis parallel to the free stream, which passes through the point $x_W = c_{rW}$, $y_W = 0$, $z_W = 0$ at the trailing edge of the wing |
| $\bar{\eta}_C = y_W/s_C$<br>$\bar{\zeta}_C = z_W \cdot \cos\alpha/s_C$ | Dimensionless aerodynamic coordinate system with the origin at $x_W = y_W = z_W = 0$ |
| $\Phi$ | Leading-edge sweep of canard or wing |

## 2.2 Aerodynamic quantities

| | |
|---|---|
| $Re = V_\infty \cdot c_{rW}/\nu$ | Reynoldsnumber |
| $V_\infty$ | Free stream velocity |
| $c_D = D/q_\infty S_W$ | Drag coefficient |
| $c_g = (g-p_\infty)/q_\infty$ | Total pressure coefficient |
| $c_L = L/q_\infty S_W$ | Lift coefficient |
| $c_m = M/q_\infty S_W \bar{c}$ | Pitching moment coefficient (reference point $N_{25W}$, nose-up positive) |
| $c_p = (p-p_\infty)/q_\infty$ | Static pressure coefficient |
| $c_q = q/q_\infty$ | Dynamic pressure coefficient |
| g | Total pressure |
| p | Static pressure |
| q | Dynamic pressure |
| $q_\infty$ | Free stream dynamic pressure |
| $\alpha$ | Angle of attack; angle between free stream and wing plane, $z_W = 0$ |
| $\nu$ | Kinematic viscosity |

## 2.3 Subscripts

| | |
|---|---|
| C | Canard |
| F | Fuselage |
| W | Wing |

## 3. Experimental set-up and test program

The experimental investigations have been carried out in the 1.3-m wind-tunnel of the Institut für Strömungsmechanik at Technische Universität Braunschweig.

### 3.1 Models

The investigations have been performed for a wing-fuselage-canard configuration, which is shown in Fig. 1. The geometric data may be taken from Tab. 1.

Wing and canard have delta planforms of aspect ratio $A_C = A_W = 2.31$ and a corresponding leading-edge sweep of $\varphi_C = \varphi_W = 60°$. In both cases symmetric parabolic arc airfoils for the root section and parabolic contours in spanwise direction have been used. The leading-edges are sharp. Both wing and canard are equipped with a tube system underneath the surface and with pressure holes in order to measure the surface-pressure distribution. A very flat fuselage has been chosen to keep the canard in position relative to the wing, to provide some variation of this position and to cover some volume necessary for the rubber tubes in the case of pressure distribution measurements. The fuselage consists of a cylindrical portion of length $l_{2F} = 8h_F$ and attached are front and rear parts of length $l_{1F} = l_{3F} = 2h_F$. Their shape has been taken as a polynomial of fourth order which meets the cylindrical part continuously with respect to slope and curvature. The wind-tunnel model was produced with $b_W = 600$ mm.

| | | |
|---|---|---|
| Canard: | Aspect ratio | $A_C = 2.31$ |
| | Leading-edge sweep | $\varphi_C = 60°$ |
| | Thickness-ratio | $(t/c_r)_C = 0.05$ |
| Wing: | Aspect ratio | $A_W = 2.31$ |
| | Leading-edge sweep | $\varphi_W = 60°$ |
| | Thickness-ratio | $(t/c_r)_W = 0.05$ |
| Fuselage: | Height-ratio | $(h/l)_F = 1/12$ |
| | Thickness-ratio | $(t/l)_F = 1/60$ |
| Combination Wing-Fuselage: | | |
| | Relative fuselage length | $l_F/b_W = 2.0$ |
| | Relative fuselage width | $t_F/b_W = 1/30$ |
| | Rear position of $N_{25W}$ | $e/l_F = 0.617$ |
| Combination Canard-Wing: | | |
| | Relative canard size | $b_C/b_W = 0.4$ |
| | Vertical position | $-0.04 \leq H \leq +0.04$ |
| | Horizontal position | $-0.08 \leq R \leq +0.16$ |
| | Setting angle | $-12° \leq \varepsilon \leq +12°$ |

Tab. 1: Geometric data of the configuration

The geometric data of the combinations wing-fuselage and canard-wing are collected in Tab. 1. The wing was added to the fuselage in such a way, that the trailing-edge of the wing coincided with the rear end of the cylindrical part of the fuselage. Concerning the canard-wing combination some variations in vertical and horizontal position as well as in setting angle of the canard were possible. The corresponding ranges may be taken from Tab. 1. A typical configuration has been chosen as a basis for comparisons. Its parameters are

$$\varepsilon = 0°, \; H = 0, \; R = 0.05$$

and it is called subsequently "normal configuration".

### 3.2 Description of the tests

The wind-tunnel investigations have been carried out at free stream velocities of $V_\infty = 30$ m/s and $V_\infty = 40$ m/s, which correspond to Reynoldsnumbers of $Re = 10^6$ and $Re = 1.4 \cdot 10^6$.

Three-component measurements have been performed for $-5° \leq \alpha \leq +40°$ with $\Delta\alpha = 2.5°$. The surface-pressure measurements have been carried out on the suction side for 7 selected angles of attack only. The flow on the upper surface of the configuration has been studied by means of oilflow patterns. For this purpose the black model surface was painted by a mixture of aluminumoxide-powder and petroleum and benzine (ratio of components : 1g aluminumoxide : $3cm^3$ petroleum : $1cm^3$ benzine) and exposed to the flow for about half a minute. The investigations, mentioned so far, were made for the normal configuration and for a large variety of other canard positions. In order to get data for a comparison with the non-interfering case these investigations were

also extended to the wing-fuselage configuration without the canard.

Flow-field measurements were carried out in planes perpendicular to the free stream using a conical five-hole probe of 2 mm diameter. These measurements were performed with the normal configuration at stations $\xi_W$ = 0, 0.3, 0.6 and 0.8 over the wing as well as at stations $\xi_W$ = 1.01 and 1.125 downstream of the wing. In order to detect interference effects the flow-field measurements were extended to the wing-fuselage configuration without canard at stations $\xi_W$ = 0.3, 0.6 and 0.8 over the wing as well as at station $\xi_W$ = 1.01 downstream of the wing. In all cases the angle of attack was $\alpha$ = 8.7°, where vortex breakdown is present neither at the wing-fuselage configuration nor at the canard-on normal configuration.

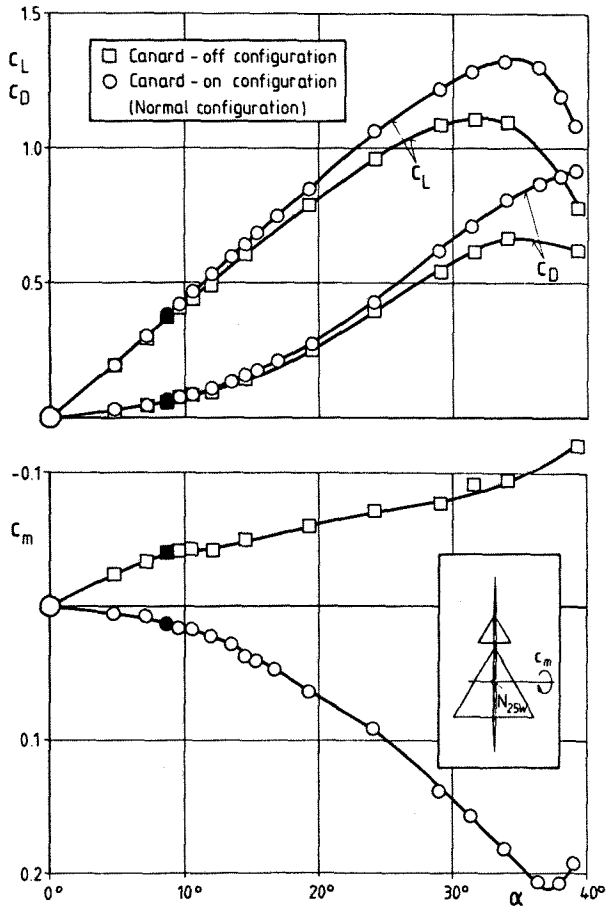


Fig. 2: Results of three-component measurements for the canard-off and the canard-on normal configuration at Re = $10^6$

## 4. Results

Major interference effects between canard and wing have been studied by means of the canard-on normal configuration and the canard-off configuration, see section 3. The results of these investigations have been published in Refs. 33 and 34. The main outcome is to be repeated here, since the knowledge of these results is essential for the understanding of the flow-field measurements presented in this paper.

At first the results of the three-component measurements for the canard-off and the canard-on normal configuration are presented in Fig. 2. For low angles of attack both configurations have nearly the same lift and drag. The addition of the canard to the wing-fuselage configuration changes a formerly nose-down pitching moment to a nose-up pitching moment. The results of the corresponding surface-pressure measurements at $\alpha$ = 8.7°, marked in Fig. 2 by the black symbols, are presented in Fig. 3: The traces of the leading-edge vortices can be detected from the suction peaks on both configurations and it can clearly be seen, that vortex breakdown does not take place at this angle of attack. A comparison between Figs. 3a and 3b reveals two characteristics of the flow around the canard configuration: The pressure distribution on the canard is very similar to the one on the wing alone and in both cases the flow is fairly conical, apart from the trailing-edge region. On the wing of the canard configuration the pressure distribution shows considerably lower suction peaks in the front part, which also lie closer to the leading-edge than in the non-interfering case. This can be seen more easily in Fig. 4 in a direct comparison of pressure distributions on the wing for the canard configuration and the non-interfering case. This comparison is taken at the same measuring stations, where the flow-field measurements presented in this paper have been performed. Fig. 4a shows at $\xi_W$ = 0.3 for the canard-off configuration a suction peak, which results from a developed vortex. On the contrary it shows for the canard configuration a suction peak, which is smaller and which lies very close to the leading edge. This "little" suction peak can only, if at all, result from a small vortex. At $\xi_W$ = 0.6 Fig. 4b shows for both cases suction peaks resulting from developed vortices. For the canard configuration the suction peak lies closer to the leading-edge than for the non-interfering case. At $\xi_W$ = 0.8, Fig. 4c, the suction peak on the canard configuration has finally reached almost size and position of the suction peak on the wing of the canard-off configuration. Fig. 4 shows, that the flow on the wing of the canard configuration is distinctly non-conical. This review ends with the presentation of the flow visualization by surface oilflow patterns at $\alpha$ = 8.7°. Fig. 5a shows the result for the non-interfering case and one can detect the traces of vortices with the aid of primary attachment and secondary separation lines. The flow is fairly conical. Fig. 5b shows a very similar pattern on the canard of the canard configuration. The streamlines on the wing of this configuration, however, are distinctly different from the non-interfering case. Primary attachment and secondary separation lines indicate, that the wing vortices start a fair distance downstream of the wing apex. On the inner portion of the leading-edge either an attached flow or a very weak flow separation is present. This delay in the formation of leading-edge vortices coincides with the smaller suction peaks of the pressure distributions, which were presented in Figs. 3 and 4a. It can also clearly be seen, that the flow on the wing of the canard configuration is highly non-conical. Fig. 5 shows again, that no vortex breakdown is present in this case.

The presentation of these results reveals, that there is a strong influence of the canard on the wing at this small angle of attack: The canard induces behind its trailing-edge a downwash field

within its span and an upwash field outside its span. The downwash field reduces the effective angle of attack in the forward and inner portion of the wing considerably. This leads to a suppression of flow separation there. The upwash field increases the effective angle of attack in the outside

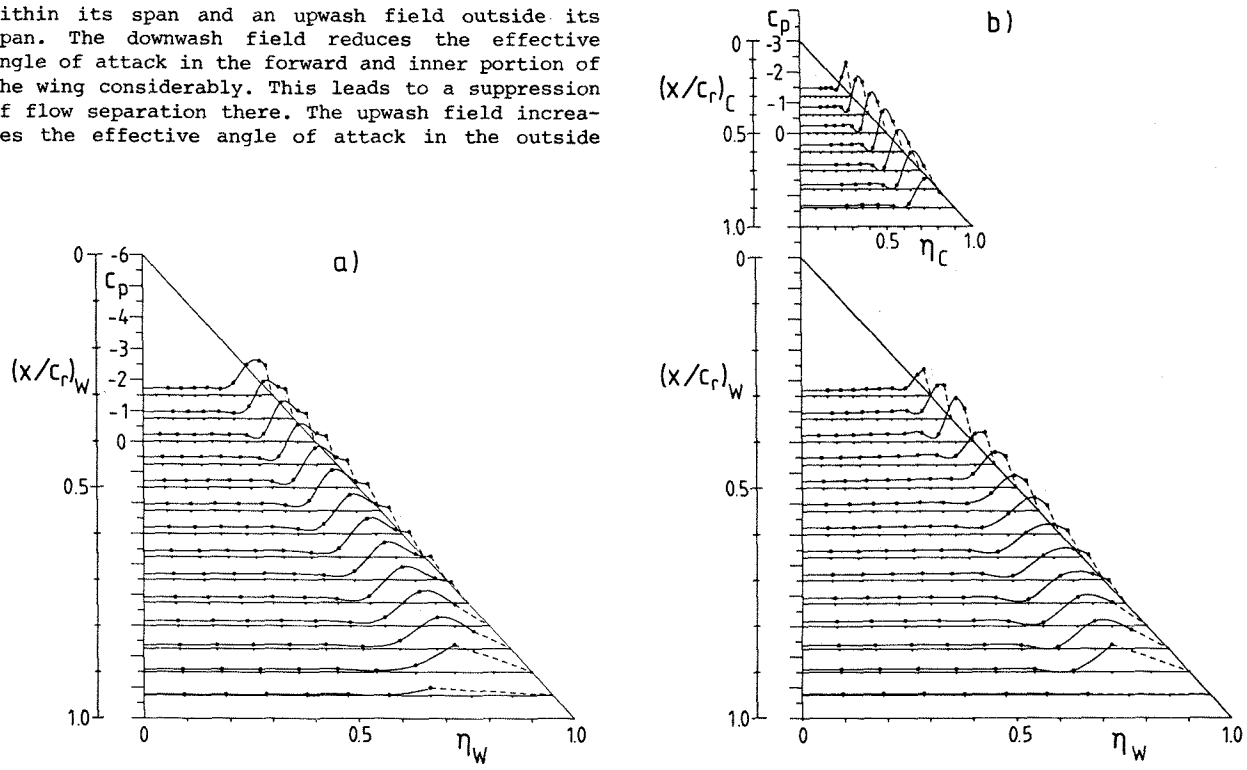


Fig. 3: Upper surface-pressure distribution at $\alpha = 8.7°$ and $Re = 1.4 \cdot 10^6$ a) canard-off configuration b) canard-on normal configuration

and rear portion of the wing, which supports flow separation there. This mechanism leads to a delayed formation of the wing vortex downstream of the wing apex. Because of the nonuniform distribution of the effective angle of attack along the leading-edge of the wing, the wing vortex is fed with vorticity in a different manner than it is known from the non-interfering case. For this reason it is possible, that the suction peak in the surface pressure distribution of the wing vortex at $\xi_w = 0.8$, see Fig. 4c, reaches almost size and location of the suction peak, which is induced by the vortex in the non-interfering case. In total, though, the wing works at a lower angle of attack than in the non-interfering case, which leads to a compensation of the additional lift at the canard through a loss of lift at the wing. Therefore both configurations have almost the same lift. At this angle of attack of $\alpha = 8.7°$ the influence of the wing on the canard was very small.

All investigations performed so far have not revealed, how the vortices coming from the canard behave over the wing of the configuration. No information could be obtained on the location and the structure of the canard wake in this region of the flow field. In order to clarify this situation extensive flow-field measurements have been carried out for the canard-on normal configuration as well as for the canard-off configuration. The investigation of both cases yields the possibility of comparison between corresponding results, so interference effects can be detected easily. Because a conventional five-hole probe was used, these measurements were limited to flow fields without vortex breakdown. The angle of attack was therefore chosen at $\alpha = 8.7°$.

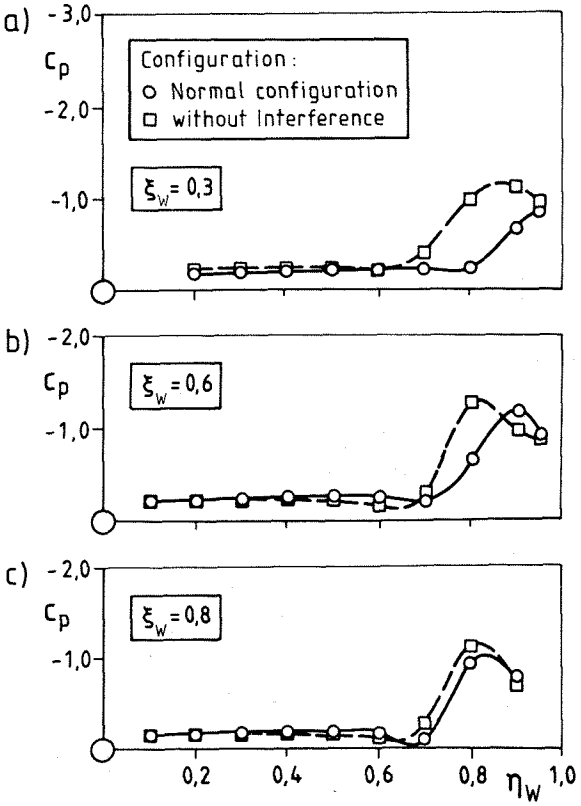


Fig. 4: Direct comparison of the upper surface-pressure distributions between the canard-off and the canard-on normal configuration at $\alpha = 8.7°$ and $Re = 1.4 \cdot 10^6$

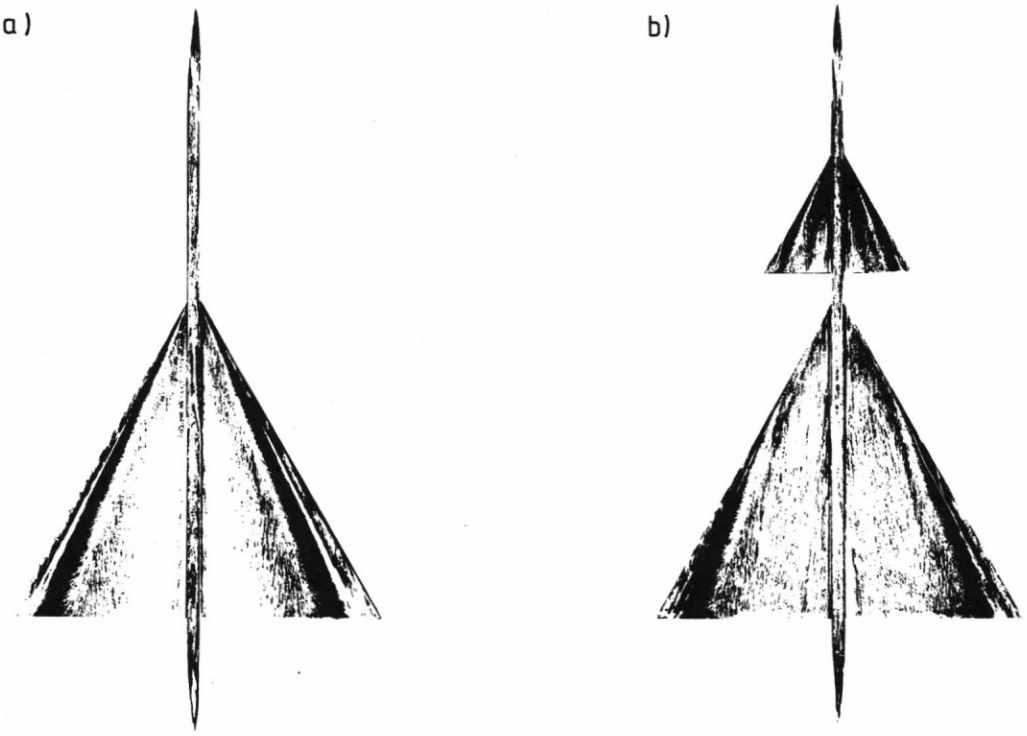


Fig. 5: Upper surface oilflow-pattern at $\alpha = 8.7°$ and $Re = 1.4 \cdot 10^6$ a) canard-off configuration b) canard-on normal configuration

4.1 Documentation of the three-dimensional flow field for the canard-off configuration

The documentation of the three-dimensional flow field for the canard-off configuration was carried out at several plans $\xi_W$ = const., see Section 3.2. The obtained results are all very similar, which is due to the "conicality" of the flow, see Figs. 3a and 5a. Therefore only results of the measurements for one plane $\xi_W$ = const. will be presented here.

Fig. 6 shows the results, which were obtained in the measuring plane $\xi_W = 0.8$. It presents lines of constant total pressure $c_g$, see Fig. 6a, lines of constant dynamic pressure $c_q$, see Fig. 6b, as well as the velocity vector component in the measuring plane, see Fig. 6c. The isobars of total pressure in Fig. 6a clearly indicate those regions of the flow field, where energy losses are present. Above the centre part of the wing as well as above the fuselage these losses emanate from the corresponding boundary layers. Local flow separation may be present in the region of the wing-fuselage junction and also on the fuselage, but these phenomena are too small and too close to the wall in order to be detected with the five-hole probe used in this investigation. The large total pressure loss region in the right-hand part of the figure is due to the leading-edge vortex system. The centre of the primary vortex is found at the location of minimum total pressure, which is at $\tilde{\eta}_W = 0.82$ and $\tilde{\zeta}_W = 0.06$. This vortex is accompanied by a secondary vortex, which is due to secondary flow separation below the primary vortex. The centre of the secondary vortex lies at approximately $\tilde{\eta}_W = 0.93$ and $\tilde{\zeta}_W = 0.02$. The secondary vortex is rather small, because the boundary layer on the wing beneath the primary vortex is turbulent. For this reason secondary flow separation occurs rather close to the leading-edge, which leads to a small secondary vortex. This effect has been investigated for delta wings by D. Hummel[37]. The location of the vorticity sheet coming from the leading-edge is indicated by a dash-dotted line. It was found by searching for relative minimum values in the total pressure distribution.

Fig. 6b shows the isobars of dynamic pressure and Fig. 6c presents the projection of the corresponding velocity vector into the measuring plane. The boundary layers on the wing and on the fuselage are clearly indicated by a loss in dynamic pressure. The centre of the primary vortex at $\tilde{\eta}_W = 0.82$ and $\tilde{\zeta}_W = 0.06$ lies in a region with a relative minimum of dynamic pressure. Also the secondary vortex is indicated by a region with low dynamic pressure. Below the centre of the primary vortex an increase of dynamic pressure is present, which leads to a relative maximum there. A second relative maximum appears above the centre of the primary vortex just outside of the region, where total pressure losses are present, see Figs. 6a and 6b. From this presentation it is obvious, that at the test Reynoldsnumber of $Re = 1.4 \cdot 10^6$ the velocity distribution within the wing vortex system is strongly influenced by viscous effects in a rather large area around the centre of the primary vortex. The increase of velocity on a line from above the primary vortex through its centre is stopped at the

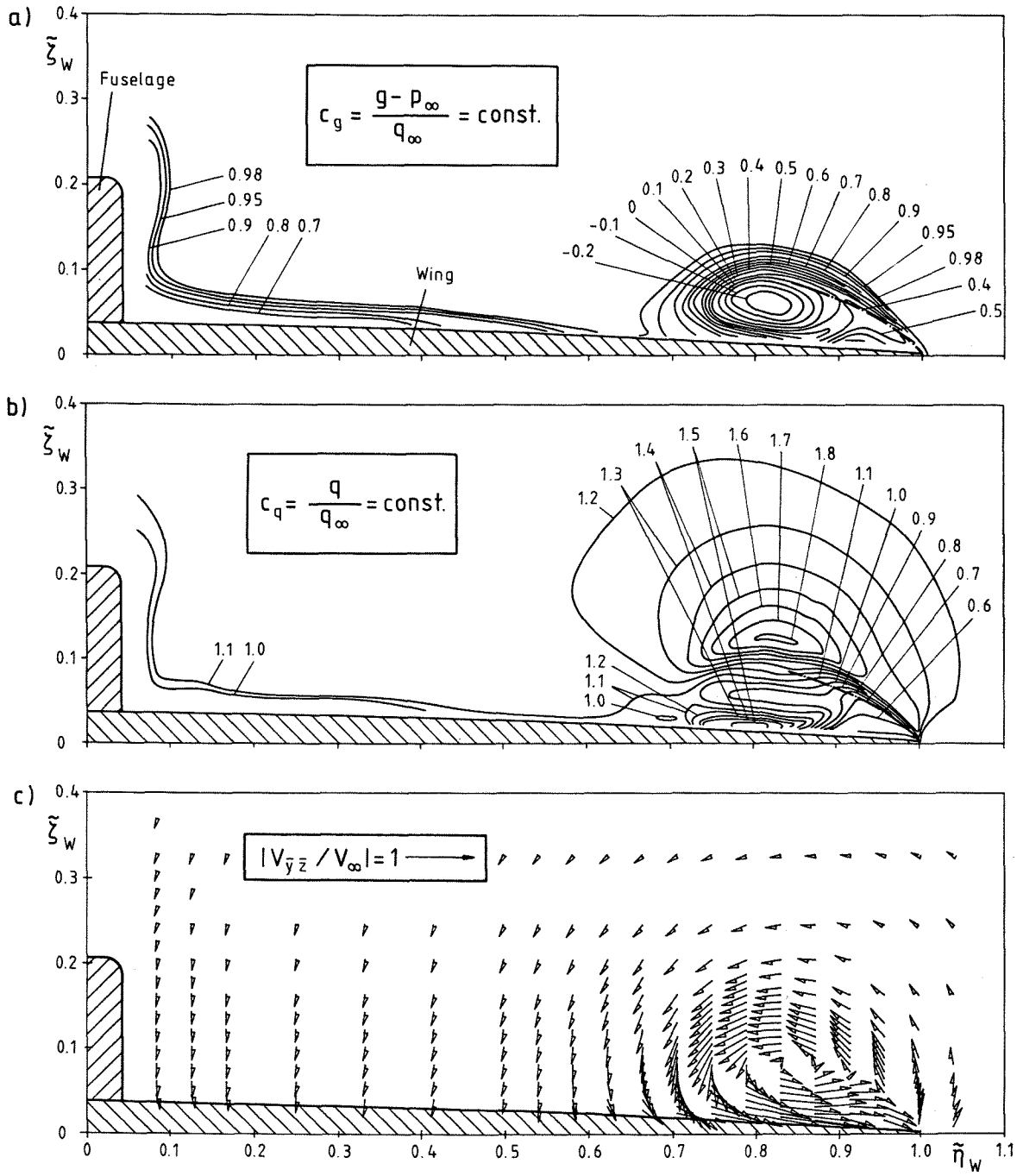


Fig. 6: Results of flow-field measurements over the canard-off configuration at $\xi_W = 0.8$, $\alpha = 8.7°$ and $Re = 1.4 \cdot 10^6$ a) total pressure isobars b) dynamic pressure isobars c) projection of the velocity vector into the measuring plane

border, where total pressure losses start to dominate the flow. Beginning there, the velocity vector decreases as the centre of the vortex is approached, see Fig. 6c. This type of velocity field is well known for trailing vortices behind wings with attached flow, which are mainly under the influence of viscous decay, as described by C.W. Oseen[38], B.G. Newman[39] and D.S. Dosanjh, E.P. Gasparek and S. Eskinazi[40] for example. The shape of the velocity field within the leading-edge vortex of this wing here is very different from the velocity field of a potential vortex. The results given in this section can now be used for comparison with the measurements above the canard configuration, which will be presented in the following section.

4.2 Documentation of the three-dimensional flow field for the canard-on configuration

The documentation of the three-dimensional flow field for the canard-on normal configuration is performed with the presentation of total pressure isobars for each measuring plane. The results of the investigations above the forward part of the wing of the normal configuration are given in Fig. 7. The first measuring plane is located at the apex of the wing at $\xi_W = 0$, which is equal to $\xi_C = 1.125$. The result is shown in Fig.7a: Regions of total pressure loss indicate the fuselage's boundary layer and the inner portion of the canard's trailing-edge wake, which is a vorticity sheet. In the region of $0.7 \leq \bar{\eta}_C \leq 1.1$ a relatively large area of total pressure losses represents the vortex system of the canard. This vortex system consists of the canard's primary vortex with its centre at $\bar{\eta}_C = 0.8$ and of the already fully developed trailing-edge vortex at $\bar{\eta}_C = 0.93$. At this measuring station the secondary vortex can hardly be detected, because it has no longer been fed with vorticity since it left the canard's trailing-edge. Both vortices though are counterrotating with respect to the primary vortex. A detailed survey on the development of a delta-wings's trailing-edge vortex and the behaviour of the secondary vortex is given by D. Hummel[37]. The results according to Refs. 33 and 34 have revealed, that there exists almost no influence of the wing on the canard at this angle of attack of $\alpha = 8.7°$. Therefore the result of Fig. 7a can be also considered as a documentation of the flow behind a delta wing without interference.

The results of the second measuring plane at $\xi_W = 0.3$ are given in Fig. 7b. Again total pressure losses indicate where the boundary layer of the fuselage is located. Detailed investigations of the flow above the fuselage were not performed. The vorticity sheet coming from the trailing-edge of the canard has "touched" the upper surface of the wing for $\eta_W \leq 0.6$. Therefore in this region a fusion of the canard's vorticity sheet with the suction side boundary layer of the wing has taken place. For $\eta_W \geq 0.6$ the vorticity sheet has again separated from the wing and it rolls into the canard's vortex system. The centre of the primary vortex of the canard can be detected at $\tilde{\eta}_W = 1.1$ and $\tilde{\zeta}_W = 0.4$ by the absolute minimum of total pressure. The trailing-edge vortex has turned around the primary vortex in the sense of rotation of the primary vortex. During this process the corresponding total pressure losses are spread out and their intensitiy is weakened considerably. At this measuring station only a very small primary vortex at the wing is present. This is due to the strong canard induced downwash at the wing leading-edge, see Fig. 4a.

The results of the third measuring plane at $\xi_W = 0.6$ are given in Fig. 7c. The process of fusion between the vorticity sheet from the canard and the suction side boundary layer of the wing has advanced. This leads to a rather thick layer of total pressure losses on the suction side of the wing. The vorticity sheet separates again from the wing at approximately $\eta_W = 0.45$ and rolls into the vortex system of the canard, which lies with the centre of its primary vortex at $\tilde{\eta}_W = 0.5$ and $\tilde{\zeta}_W = 0.31$. The pressure losses associated with the trailing-edge vortex have rotated further around the primary vortex in the sense of rotation of the primary vortex. The level of these pressure losses has also further decreased. At this station the canard vortex system is completely within the local wing span and the induced velocities of this system at the leading-edge of the wing are therefore directed upwards. This situation favours flow separation at the wing leading-edge and a relatively large area of total pressure losses associated with a wing vortex system can be found above the wing. The centre of the primary vortex lies at $\tilde{\eta}_W = 0.87$ and $\tilde{\zeta}_W = 0.06$, whereas the centre of the corresponding secondary vortex lies at $\tilde{\eta}_W = 0.95$ very close to the wing surface. The small secondary vortex indicates that the flow beneath the primary vortex is turbulent. The relative size of the wing vortex system is considerably smaller than in the non-interfering case, as it is revealed in a comparison with Fig. 6a, which is valid since the flow over the wing without canard is fairly conical.

Fig. 8 presents the results of the flow field measurements for the fourth station at $\xi_W = 0.8$, which are presented in the same manner like it was done for the non-interfering case at the same measuring station in Fig. 6. Fig. 8a shows the isobars of total pressure. Compared with the results of the upstream station at $\xi_W = 0.6$, see Fig. 7c, no principal differences can be found. Only the relative size of the wing vortex at $\xi_W = 0.8$ has grown slightly, but it has not yet reached the relative size of the wing vortex in the non-interfering case, which is revealed through a comparison between Figs. 8a and 6a. Fig. 8b shows the isobars of dynamic pressure. The wing vortex is dominated by strong viscous effects in the same manner as it was found for the non-interfering case, see Fig. 6b. At the location of the canard vortex system a relatively flat distribution of dynamic pressure with small gradients can be found. The projection of the local velocity vector into the measuring plane in Fig. 8c shows a distinctly rotating velocity field, which still indicates the location of the canard vortex over the wing. The presentation of the results from above the wing of the normal configuration shows, that the canard vortex system is moved inwards and downwards towards the wing surface as it passes downstream.

Fig. 9 presents the results of the flow field measurements behind the wing. The situation just downstream of the trailing-edge at $\xi_W = 1.01$ is given in Fig. 9a. The process of fusion between the vorticity sheet from the canard and the suction side boundary layer of the wing has led to a rather thick wake coming from the trailing-edge of the wing for $\bar{\eta}_W \leq 0.45$. The vorticity sheet of the canard separates from this wake and rolls into the canard vortex system as observed earlier. The total pressure losses of the canard vortex system still show regions, which can be associated with the canard's trailing-edge vortex. The relative size of the wing vortex has grown again. A comparison with Fig. 6a reveals, that the wing vortex has now reached the same relative size as the wing vortex of the non-interfering case. The canard induced upwash along the wing leading-edge causes an increase of effective angle of attack there, which in turn supports flow separation at the leading-edge. This mechanism is responsible for the growth along the leading-edge from the almost negligibly small vortex at $\xi_W = 0.3$, see Fig. 7b, up to the same relative size of the vortex of the non-interfering case, which is reached at the trailing-edge of the

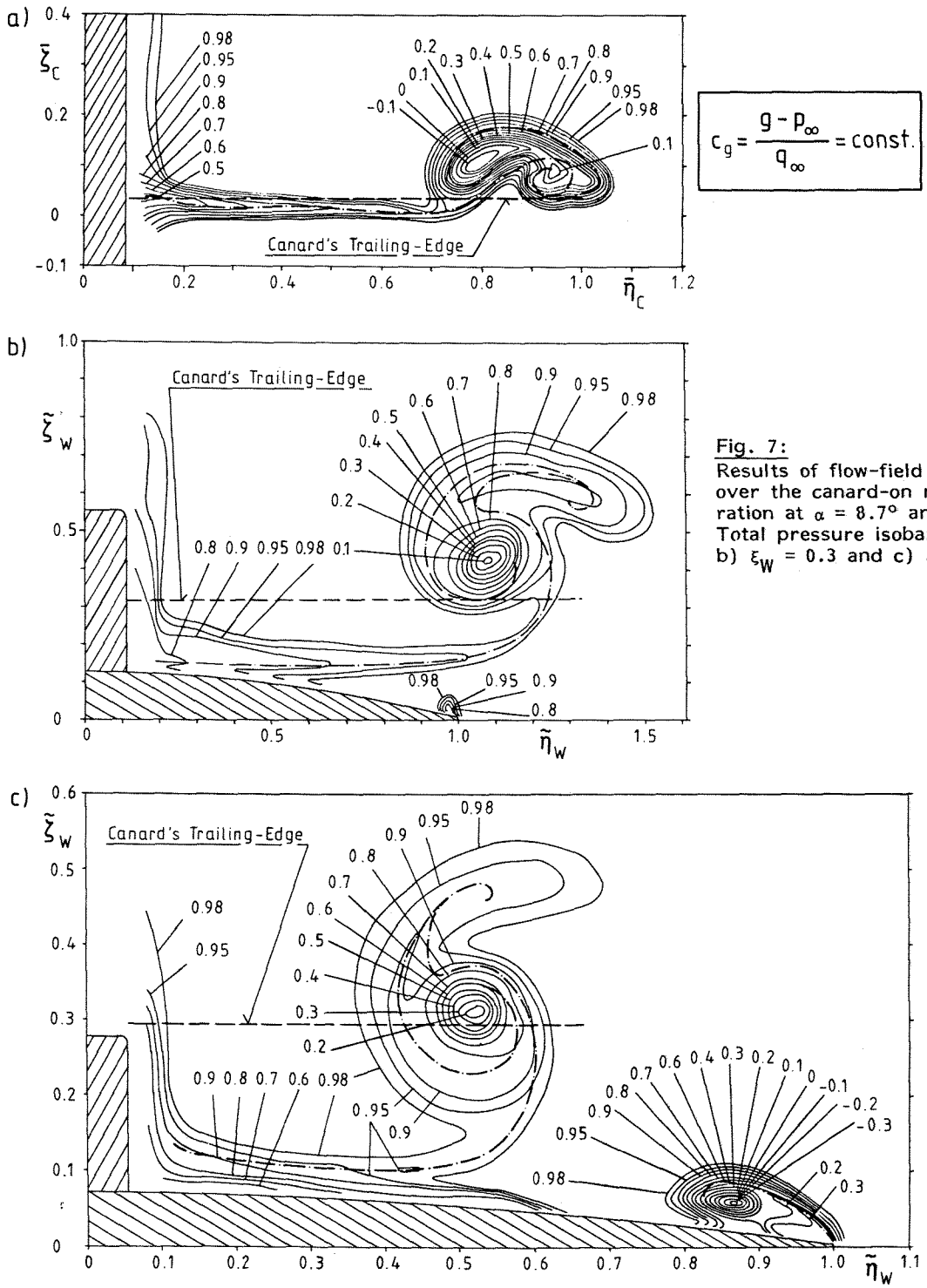


Fig. 7:
Results of flow-field measurements over the canard-on normal configuration at $\alpha = 8.7°$ and $Re = 1.4 \cdot 10^6$. Total pressure isobars at a) $\xi_W = 0$, b) $\xi_W = 0.3$ and c) $\xi_W = 0.6$

wing, see Figs. 9a and 6a. This means also, that the wing vortex of the canard configuration is fed with vorticity in a different manner along the leading-edge than in the non-interfering case. The presentation of the preceding figures also indicates, that the flow over the canard configuration is highly non-conical.

The results of the measurements in the last plane at $\xi_W = 1.125$ are presented in Fig. 9b. Concerning the canard vortex system principal changes have not occurred. The wing primary vortex is now accompanied by a distinct counter-rotating trailing-edge vortex. At $\eta_W = 0.42$ one can detect a small relative minimum of total pressure in the wake coming from the wings's trailing-edge, which results from the separation process between the vorticity sheet from the canard and the suction side boundary layer of the wing. This relative minimum may represent the total pressure losses of a small vortex, which lies inside the trailing-edge wake. This vortex may also be present already above the wing at $\eta_W = 0.47$, see Fig. 8a. The corresponding oil flow pattern supports this idea, see Fig.

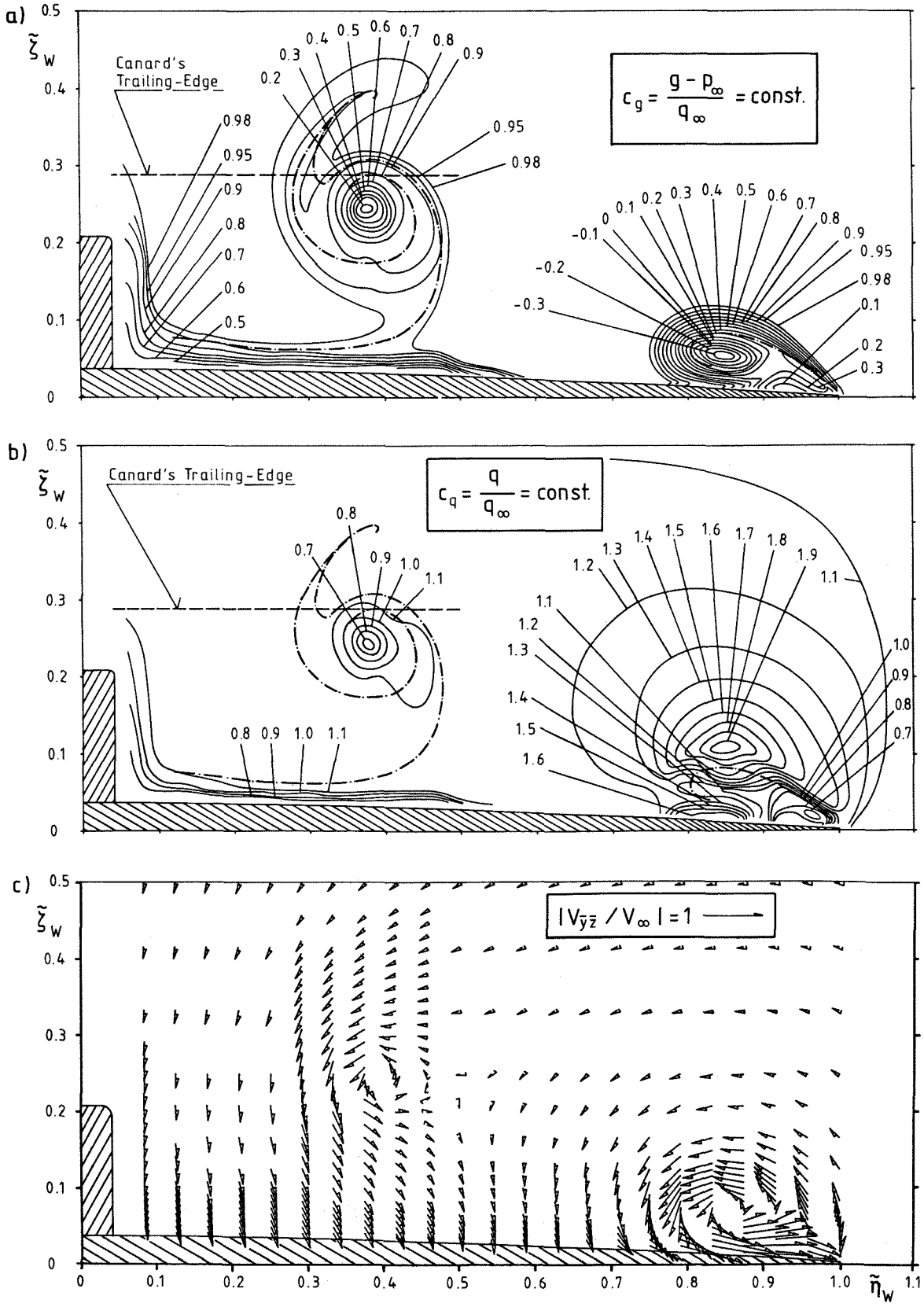


Fig. 8: Results of flow-field measurements over the canard-on normal configuration at $\xi_W = 0.8$, $\alpha = 8.7°$ and $Re = 1.4 \cdot 10^6$ a) total pressure isobars b) dynamic pressure isobars c) projection of the velocity vector into the measuring plane

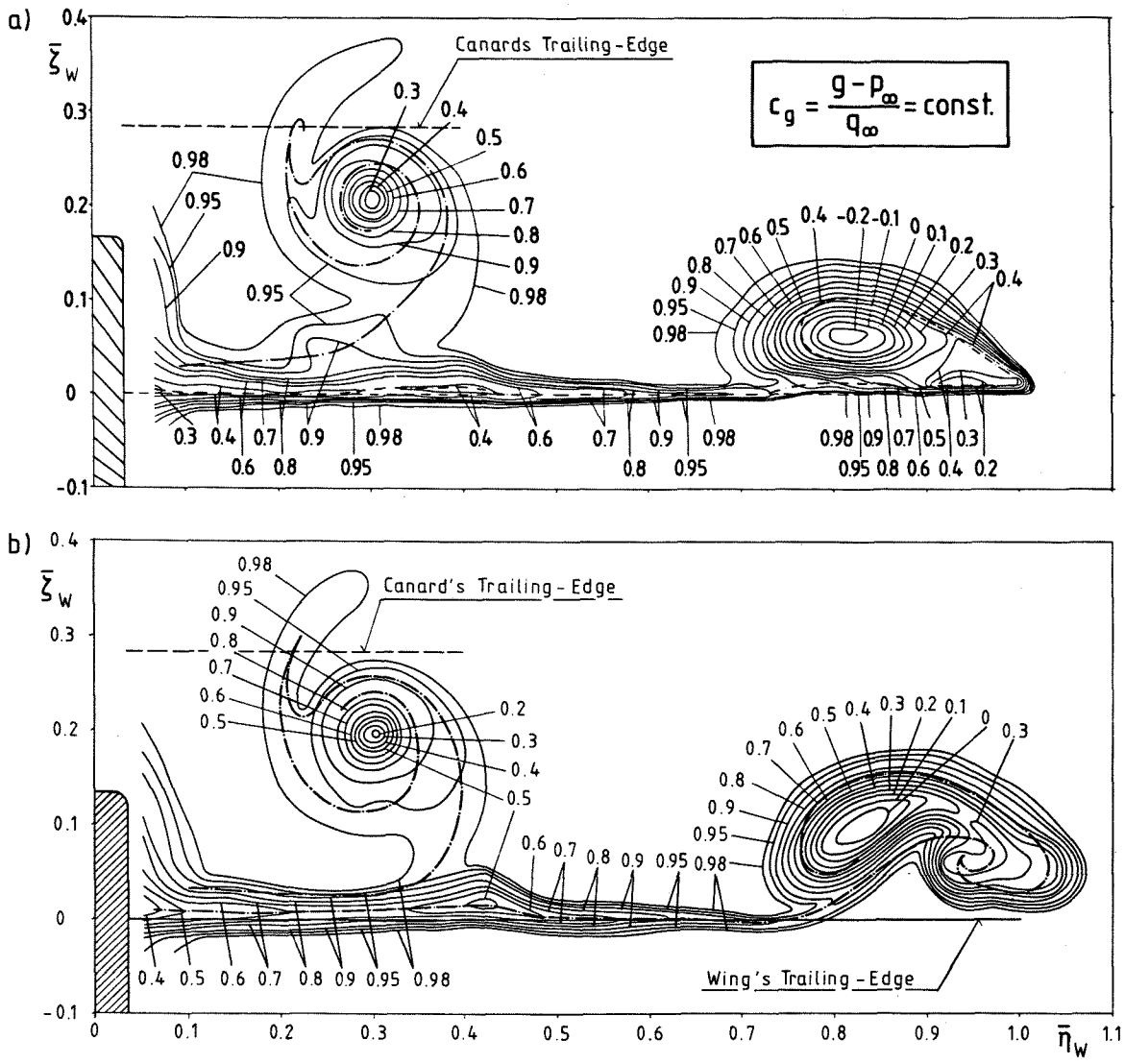


Fig. 9: Results of flow-field measurements behind the canard-on normal configuration at $\alpha = 8.7°$ and $Re = 1.4 \cdot 10^6$. Total pressure isobars at a) $\xi_W = 1.01$ and b) $\xi_W = 1.125$

5b: In the vicinity of the trailing-edge at approximately $\eta_W = 0.42$ a slight convergence of the wall streamlines is observed, which might be an indication of small and local flow separation. Unfortunetly this phenomenon is too small in order to be resolved properly with the five-hole probe in use or even with the given surface-pressure distribution measurements, because the distance between two pressure tabs of $\Delta\eta_W = 0.1$ is relatively large.

Another outcome of the flow-field measurements is the distribution of the static pressure in each measuring plane. Because of limited space these results will not be presented here. Only a conclusive overview is given in Fig. 10. This figure represents the distribution of minimum static pressure in each measuring plane as a function of the longitudinal coordinate $\xi_W$. Minimum static pressure always occurs in the centre of the primary vortices. Fig. 10 shows for the non-interfering case a constant value of minimum static pressure in the centre of the primary vortex over the wing, which experiences a steep positive pressure gradient as

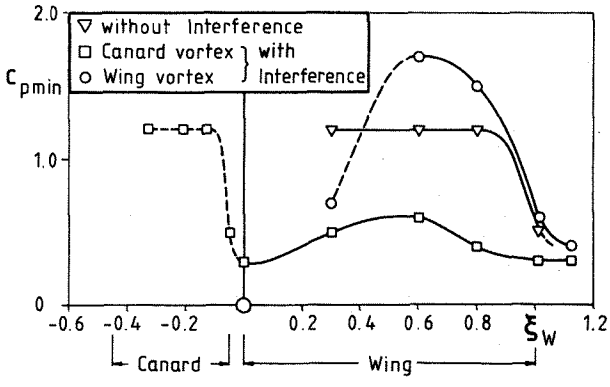


Fig. 10: Distribution of minimum static pressure in the centre of the vortices of the canard-off and canard-on normal configuration at $\alpha = 8.7°$ and $Re = 1.4 \cdot 10^6$

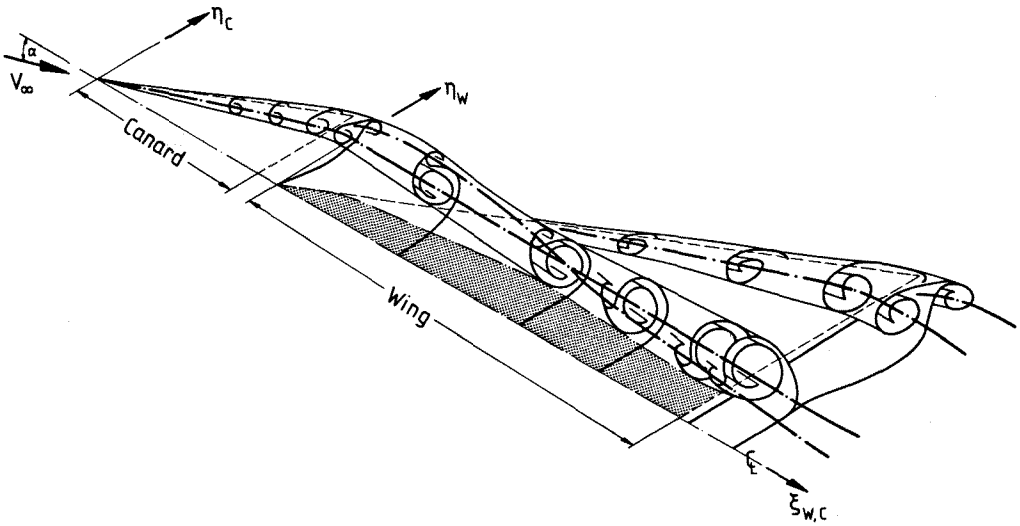


Fig. 11: Schematic overview of the flow field above the canard-on normal configuration at low angle of attack and inviscid flow

the trailing-edge is approached. This behaviour again indicates, that the flow around the canard-off configuration is fairly conical above the forward part of the wing. It is known from Refs. 33 and 34, that the flow over the canard is not significantly influenced by the wing at this angle of attack. Therefore the distribution of minimum static pressure for the non-interfering case is also used for the canard of the normal-configuration, see Fig. 10. Through this method one achieves the distribution of minimum static pressure in the centre of the canard's primary vortex from above the canard to a point downstream of the wing trailing-edge: Over the canard the already discussed pressure distribution is present. From the trailing-edge of the canard to the apex of the wing the the minimum static pressure increases further. Over the wing the value of minimum static pressure within the canard's primary vortex decreases and towards the trailing-edge of the wing the value of minimum static pressure increases again, but not as steep as in the vicinity of the canard's trailing-edge. The decrease of minimum static pressure above the wing is caused by the wing flow. It is due to the lift, which is generated by the wing. This decrease of static pressure can be interpreted as an acceleration of the vortical flow coming from the canard. At larger angles of attack, when the canard vortices burst above the canard, this situation is responsible for the process of restoring the burst canard vortices back into a non-burst state. This phenomenon is documented in detail in Refs. 33 and 34 already. Finally the distribution of minimum static pressure of the wing vortex of the normal-configuration shows much lower values than for the non-interfering case. This again is an illustration of the nonuniform vorticity feeding mechanism of the wing vortex at the canard configuration.

At the end of this documentation Fig.11 gives a global overview of the three-dimensional flow field above the canard-on normal configuration as it is understood by the authors. For this presentation the effects of viscosity have been neglected, wing and canard are considered to be flat plates and no fuselage is taken into account. Fig. 11 illustrates how the canard vortex system develops and how this system is located above the wing. The shaded area, which lies in Fig. 11 towards the centre line of the configuration, shows that region of the wing, where the vorticity sheet of the canard joins the suction side boundary layer of the wing, as documented in the preceding figures. This means for the simplified case of Fig. 11, that the free vorticity sheet coming from the canard joins the wing-fixed vorticity sheet. Therefore in the shaded region of the wing instead of two only one combined vorticity sheet is present. Finally behind the wing one can clearly see a system of four vortices on the right-hand side of the configuration. These vortices were generated during the course of the flow and there is one primary vortex each for canard and wing, which is accompanied by a corresponding trailing-edge vortex after having left either canard's or wings's trailing-edge. These vortices are already existing in non-viscous flow. Fig. 11 demonstrates the complexity of the flow and it gives a guideline for numerical simulators in the sense, that it shows all those features of the flow, which should be an outcome of an inviscid flow theory.

## 5. Conclusions

Comprehensive aerodynamic investigations have been carried out on a close-coupled A = 2.31 delta-canard configuration at low speed. Results of three-component, surface-pressure and flow-field measurements as well as oilflow patterns are presented for the canard-off and the canard-on configuration. The flow-field measurements were carried out at $\alpha = 8.7°$, where vortex breakdown is not present over the configuration.

Major findings of these investigations are:

1) The vortices existing in both cases are strongly influenced by viscous effects at the test Reynoldsnumber of $Re = 1.4 \cdot 10^6$. In regions with total pressure losses, $c_q < 1$, a considerable decrease of flow velocity is present, if the centre of a vortex is approached. In a numerical simulation this phenomenon will turn out by taking into account viscous effects properly.

2) The canard vortex system passes the wing leading-edge relatively high above the configuration. Through wing influence this system is

moved above the wing inward towards the centre of the configuration and also downward towards the wing surface. The canard vortex system consists of the canard's primary vortex as well as the corresponding trailing-edge vortex, which develops just downstream of the canard. This vortex system keeps its structure up to stations downstream of the wing trailing-edge.

3) Due to induced velocities the vorticity sheet coming from the canard's trailing-edge is moved towards the upper wing surface, which leads to a fusion between this vorticity sheet and the suction side boundary layer in the inner portion of the wing surface. In non-viscous flow this process is equivalent to a fusion of the free canard vorticity sheet with the wing bound vorticity sheet. Beneath the canard vortex the vorticity sheet of the canard separates from the wing surface again and it rolls into the canard vortex system.

4) Because of the canard's downwash at the leading-edge in the forward, inner portion of the wing the effective angle of attack is reduced there considerably. This leads to a suppression of flow separation and the formation of the wing leading-edge vortex is therefore delayed until the canard's induced upwash supports flow separation. Because of the nonuniform distribution of the effective angle of attack along the leading-edge of the wing, the wing vortex is fed with vorticity in a different manner than it is known from the non-interfering case. Nevertheless at the wing trailing-edge the same relative size and position of the wing vortex is reached as in the non-interfering case. The wing vortex system of the canard configuration is therefore highly non-conical.

## 6. References


1 H. Behrbohm: Basic low speed aerodynamics of the short-coupled canard configuration of small aspect ratio. Saab TN 60 (1965).

2 W.R. Bates: Low-speed static longitudinal stability characteristics of a canard model having a 60° triangular wing and horizontal tail. NACA RM L9H17 (1949).

3 W.R. Bates: Low-speed static lateral stability characteristics of a canard model having 60° triangular wing and horizontal tail. NACA RM L9J12 (1949).

4 J.W. Draper: Low-speed static stability characteristics of a canard model with a 45° sweptback wing and a 60° triangular horizontal control surface. NACA RM L50G11 (1950).

5 J.L. Johnson Jr.: A study of the flow field behind the triangular horizontal tail of a canard airplane at approximately the vertical-tail location by means of a tuft grid. NACA RM L52H11 (1952).

6 D.L. Burrows: Large-scale low-speed wind-tunnel tests of a model having a 60° delta horizontal canard control surface and wing to obtain static-longitudinal-stability and canard-surface hinge-moment data. NACA RM L54D16a (1954).

7 W.C. Sleeman Jr.: Investigation at high subsonic speeds of the static longitudinal and lateral stability characteristics of two canard airplane configurations. NACA RM L 57J08 (1957).

8 W.I. Scallion: Low-speed static longitudinal and lateral aerodynamic characteristics of a model with a low-aspect-ratio variable-incidence wing and with a free-floating and a programed high-lift canard control. NASA TN-D 1381 (1962).

9 D.W. Lacey, St.J. Chorney: Subsonic aerodynamic characteristics of close-coupled canards with varying area and position relative to a 50° swept wing. Naval Ship Research and Development Center, Techn. Note AL-199 (1971).

10 J.R. Krouse: Effects of canard planform on the subsonic aerodynamic characteristics of a 25° and a 50° swept-wing research aircraft model. Naval Ship Reseach and Development Center, Evaluation Report AL-91 (1972).

11 J. Ottensoser: Wind tunnel data on the transonic aerodynamic characteristics of close coupled canards with varying planform position and deflection relative to a 50° swept wing. Naval Ship Research and Development Center, Test Report AL-88 (1972).

12 D.W. Lacey: Transonic characteristics of close-coupled canard and horizontal tail installed on a 50 degree sweep research aircraft model. Naval Ship Research and Development Center, Evaluation-Report AL-81 (1972).

13 B.B. Gloss. L.W. McKinney: Canard-wing lift interference related to maneuvering aircraft at subsonic speeds. NASA TM X-2897 (1973).

14 B.B. Gloss: Effect of canard location and size on canard-wing interference and aerodynamic-center shift related to maneuvering aircraft at transonic speeds. NASA TN D-7505 (1974).

15 W.P. Henderson: The effect of canard and vertical tails on the aerodynamic characteristics of a model with a 59° sweptback wing at a Mach number of 0.30. NASA TM X-3088 (1974).

16 B.B. Gloss: The effect of canard leading-edge sweep and dihedral angle on the longitudinal and lateral aerodynamic characteristics of a close-coupled canard-wing configuration. NASA TN D-7814 (1974).

17 B.B. Gloss: Effect of wing planform and canard location and geometry on the longitudinal aerodynamic characteristics of a close-coupled canard wing model at subsonic speeds. NASA TN D-7910 (1975).

[18] R.P. Boyden: Subsonic dynamic stability characteristics of two close-coupled canard-wing configurations. NASA TP-1291 (1978).

[19] B.B. Gloss: Effect of camber on the trimmed lift capability of a close-coupled canard-wing configuration. NASA Techn. Memo. 78686 (1978).

[20] B.B. Gloss, E.J. Ray, K.E. Washburn: Effect of canard vertical location, size and deflection on canard-wing interference at subsonic speeds. NASA Techn. Memo. 78790 (1978).

[21] R.B. Eberle, R.T. Stancil, W.C. Fowler: A critical review of canard relative to aft horizontal tail based on low- and high-speed tunnel tests of a fighter/attack configuration. AIAA-Paper No. 71-8 (1971).

[22] S.E. Goldstein, C.P. Combs: Trimmed drag and maximum flight efficiency of aft tail and canard configurations. AIAA-Paper No. 74-69 (1974).

[23] H. John, W. Kraus: High angle of attack characteristics of different fighter configurations. AGARD-CP-247 (1978), 2-1 to 2-12.

[24] W. Kraus: Delta canard configuration at high angle of attack. Z. Flugwiss. Weltraumforsch. 7 (1983), 41-46.

[25] B.B. Gloss, D.D. Miner: Flow visualization study of close-coupled canard-wing and strake-wing configurations. NASA TM X-75663 (1975).

[26] D.J. Lorincz: Flow visualization study of the HIMAT RPRV. NASA-CP-163094 (1980).

[27] J. Er-El, A. Seginer: Vortex trajectories and breakdown on wing-canard configurations. J. Aircraft 22 (1985), 641-648.

[28] R. Gallington, G. Sisson: Flow visualization using a computerized data aquisition system. Preprints of the Contributed Papers, International Symposium on Flow Visualization, 9. - 12. Sept. 1980, Ruhr Universität Bochum (1980), 134-141.

[29] K.E. Griffin: Measurement of wake interactions of a canard and a forward swept wing. USAFA-TN-82-4 (1982), US Air Force Academy, Colorado Springs 80840, Colorado.

[30] K.E. Griffin, E.C. Haerter, B.R. Smith: Wake characteristics and intreractions of the canard/wing lifting surface configuration of the X-29 forward swept wing flight demonstrator. USAFA-TN-83-7 (Aug. 1983), US Air Force Academy, Colorado Springs 80840, Colorado.

[31] K.E. Griffin, F.M. Jonas: Wake characteristics and interactions of the canard wing lifting surface configuration of the X-29 forward swept wing flight demonstrator. AIAA-Paper 83-1835 (1983).

[32] L. Hjelmberg: Test on a 55° and 65° delta wing at FFA. Proceedings of International Vortex Flow Experiment on Euler Code Validation, Stockholm October 1-3 1986, Flygtekniska Forsöksanstalten, Bromma, Schweden (1986), 89-106.

[33] D. Hummel, H.-Chr. Oelker: Vortex interference effects on close-coupled canard configurations in incompressible flow. Proceedings of International Vortex Flow Experiment on Euler Code Validation, Stockholm October 1-3 1986, Flygtekniska Forsöksanstalten, Bromma, Schweden (1986), 47-61 .

[34] H.-Chr. Oelker, D. Hummel: Experimentelle Untersuchungen an Entenkonfigurationen. DGLR-Bericht 86-03 (1986), 172-191.

[35] D. Hummel: Documentation of separated flows for computational fluid dynamics validation. AGARD-CPP-437 (1988), P18-1 to P18-24

[36] H.-Chr. Oelker: Aerodynamische Untersuchungen an kurzgekoppelten Entenkonfigurationen. Dissertation TU Braunschweig (in Preparation).

[37] D. Hummel: On the vortex formation over a slender wing at large angles of incidence. AGARD-CP-247 (1978), 15-1 to 15-17.

[38] C.W. Oseen: Über Wirbelbewegung in einer reibenden Flüssigkeit. Ark. för. Mat., Astron. och Fys. 7 (1911) Nr. 14, 1-13.

[39] B.G. Newman: Flow in a viscous trailing vortex. The Aeronautical Quarterly 10 (1959), 149-162.

[40] D.S. Dosanjh, E.P. Gasparek, S. Eskinazi: Decay of a viscous trailing vortex. The Aeronautical Quarterly 13 (1962), 167-188.